Environment International 131 (2019) 105024

Contents lists available at ScienceDirect

Environment International

journal homepage: www.elsevier.com/locate/envint

Precise control of iron activating persulfate by current generation in an electrochemical membrane reactor

Simiao Wu[a,b], Guannan Liang[a], Xiaohong Guan[c], Guangren Qian[a], Zhen He[b,*]

[a] School of Environmental and Chemical Engineering, Shanghai University, Shanghai 200444, PR China
[b] Department of Civil and Environmental Engineering, Virginia Polytechnic Institute and State University, Blacksburg, VA 24061, USA
[c] College of Environmental Science and Engineering, Tongji University, Shanghai 200092, PR China

ARTICLE INFO

Handling Editor: Yong-Guan Zhu

Keywords:
Persulfate activation
Precise control
Current generation
Electrochemical membrane reactor
Advanced oxidation process

ABSTRACT

Activated persulfate (PS) oxidation is promising for contaminant removal but a lack of controllable activation can lead to a loss of reagents and thus low contamination degradation. Herein, we have proposed and investigated an innovative method to control PS activation by introducing ion exchange membrane into electrochemically activated PS. This electrochemical membrane reactor (EMR) could precisely control PS activation by adjusting electrical current for slow release of Fe^{2+}, and also avoid direct contact between PS and a sacrificial anode electrode (iron electrode)/an alkaline cathode solution. It was found that the PS decomposition rate constant was linearly increased by increasing the applied current (R^2 = 0.988). The rate of the released Fe^{2+} also exhibited a linear relationship with the applied current (R^2 = 0.995). Compared to one-time dosage of Fe^{2+}, the EMR-based slow-release process had higher contamination degradation and better PS utilization (molar ratio of the decomposed PS to the migrated Fe, 1.04 ± 0.01:1), thereby minimizing the waste of both reaction reagents and generated radicals. The EMR was also employed to degrade a representative dye contaminant in a controllable manner and achieved 95.7 ± 0.7% removal percentage with PS dosage of 3.0 g L^{-1} within 20 min. This study is among the earliest to explore effective approaches for precisely controlling PS activation and subsequent oxidation of contaminants.

1. Introduction

Advanced oxidation processes (AOPs) based on activated persulfate (PS, $S_2O_8^{2-}$) are an emerging technology for treating recalcitrant compounds in groundwater and industrial wastewater (Hung et al., 2016; Pu et al., 2018). At room temperature, PS is much more stable than H_2O_2 (which is used in Fenton or Fenton-like processes), and thus can be handled and stored more conveniently and safely (Wang and Wang, 2018). Sulfate radicals ($SO_4^{\bullet-}$) generated from PS activation (E^0 = 2.1 V) has a higher redox potential (E^0 = 2.5–3.1 V) than hydroxyl radical (·OH, E^0 = 1.9–2.7 V) (Oh et al., 2016) and orders of magnitude longer half-life period ($t_{1/2}$ = 30–40 μs vs $t_{1/2}$ = 0.02 μs of •OH) (Pikaev and Zolotarevskii, 1967). Sulfate radicals can also form reactive hydroxyl radicals (Eqs. (1) and (2); Wojnárovits and Takács, 2019; Hayon et al., 1972) (Li et al., 2017). Several previous studies have suggested that ·OH could be the dominant reactive species in iron-activated persulfate systems (Ahmad et al., 2012; Liang and Su, 2009; Tang et al., 2018). In addition, $SO_4^{\bullet-}$ induced AOPs are active within a wide range of pH (Jawad et al., 2018), which makes it more selective toward electron-rich organic contaminants and unsaturated bonds, for example the molecules of azo dyes containing an azo bond (−N=N−) associated with benzene that is highly resistant to natural degradation (N. Liu et al., 2018; Lu et al., 2016). In general, PS can be activated by heat (L. Wang et al., 2017; Zhu et al., 2018), UV radiation (Eq. (3)) (An et al., 2015; Tian et al., 2018), and transition metals like iron (Liu et al., 2017; Y. Zhang et al., 2018) through an electron transfer process (Eq. (4); Kamagate et al., 2018). Both heating and UV activation could be energy intensive (Devi et al., 2016; Rosenfeldt et al., 2006; Silveira et al., 2017), although UV Light emitting diodes (LEDs) may provide energy-efficient light sources (Jo and Tayade, 2014). Iron is a more attractive activator because of its large abundance, high efficiency, and environmentally-friendly properties (Zhen et al., 2018).

$$SO_4^{\bullet-} + H_2O \rightarrow SO_4^{2-} + \bullet OH + H^+ \quad (k = 6.6 \times 10^2\ mol^{-1}\ L\ s^{-1}) \tag{1}$$

$$SO_4^{\bullet-} + OH^- \rightarrow SO_4^{2-} + \bullet OH \quad (k = 5.5 - 5.7 \times 10^7\ mol^{-1}\ L\ s^{-1}) \tag{2}$$

$$S_2O_8^{2-} \xrightarrow{heat\ or\ UV} 2SO_4^{\bullet-} \tag{3}$$

* Corresponding author.
E-mail address: zhenhe@vt.edu (Z. He).

https://doi.org/10.1016/j.envint.2019.105024
Received 25 June 2019; Received in revised form 14 July 2019; Accepted 15 July 2019
Available online 26 July 2019
0160-4120/ © 2019 The Authors. Published by Elsevier Ltd. This is an open access article under the CC BY-NC-ND license (http://creativecommons.org/licenses/BY-NC-ND/4.0/).

$$S_2O_8^{2-} + Fe^{2+} \rightarrow SO_4^{\bullet -} + SO_4^{2-} + Fe^{3+} \quad (k = 2.7 \times 10^1\ mol^{-1}\ L\ s^{-1}) \quad (4)$$

Excess input of PS is usually required at almost 50–200 times the molar amount of contaminants (Li et al., 2016; Lin et al., 2014; Shang et al., 2017b; Wang and Wang, 2018; Wu et al., 2018), and a greater molar amount of iron is added to activate PS (varied from 1.25:1 to 4:1) (Al-Shamsi and Thomson, 2013; Wu et al., 2018; Zhen et al., 2018). The generated $SO_4^{\bullet -}$ could be scavenged by excess Fe^{2+} (Eq. (5); Yu et al., 2018) with rapid oxidation of Fe^{2+} to Fe^{3+}, resulting in the waste of generated radicals and some added Fe^{2+} (Lee et al., 2009; Vicente et al., 2011). Thus, the loss of PS and the low utilization efficiency of radicals are the key challenges of iron-based PS activation. To improve utilization efficiency of PS, chelated iron has been employed by increasing iron solubility and decreasing the reaction rate of Fe^{2+} (Liang et al., 2004). However, the chelating agents could react with PS and injecting chelating agents would introduce new pollutants (Han et al., 2015). Zero-valent iron and iron oxides have also been investigated as heterogeneous catalysts for more efficient use of Fe^{2+} (Kim et al., 2018; Yun et al., 2017), but the surface of those catalysts is not stable and may be easily deactivated; furthermore, catalyst recycling also remains a major issue to address (Chen et al., 2018; Yin et al., 2018).

$$Fe^{2+} + SO_4^{\bullet -} \rightarrow SO_4^{2-} + Fe^{3+} \quad (k = 4.6 \times 10^9\ mol^{-1}\ L\ s^{-1}) \quad (5)$$

In situ electrochemically activated persulfate (EAP), which uses a sacrificial iron anode for continuous generation of Fe^{2+} by applying a positive current (Eq. (6)), is of great interest to improving the utilization of both Fe^{2+} and PS (Song et al., 2018; L. Zhang et al., 2018). EAP can manipulate the PS reactivity through controlling anodic electrochemical corrosion (ECC) and Fe^{2+} supply, according to that the production rate of Fe^{2+} is proportional to electrical current based on Faraday law (Yuan et al., 2014). By reversing polarity, the production of Fe^{2+} could be suppressed to halt PS reactivity (Yuan et al., 2014). However, chemical corrosion (CC) of iron electrodes via direct contact with PS is inevitable (Eq. (7)) (Li et al., 2019; Oh et al., 2009), and will negatively affect PS activation. In addition, OH^- production (Eq. (8)) on the cathode due to oxygen reduction reaction will cause pH increase and thus Fe^{2+} precipitation (Li et al., 2018), which may deactivate iron catalysts and also accelerate the consumption of generated $SO_4^{\bullet -}$ (Eq. (2)) (Cai et al., 2016).

$$Fe^0 - 2e^- \rightarrow Fe^{2+} \quad (6)$$

$$Fe^0 + S_2O_8^{2-} \rightarrow Fe^{2+} + 2SO_4^{2-} \quad (7)$$

$$2H_2O + 2e^- \rightarrow H_2 + 2OH^- \quad (8)$$

To better control PS activation, we introduced ion exchange membrane into EAP, forming an electrochemical membrane reactor (EMR) consisting of three chambers (anode, reaction and cathode) separated by two pieces of cation exchange membrane (CEM) (Fig. 1). Placing an iron electrode in the anode chamber avoids direct contact with wastewater and oxidizing agent PS, both of which are in the reaction chamber (middle chamber). In this way, electrical current is the only factor to generate Fe^{2+} via ECC and drive Fe^{2+} ions to move from the anode chamber to the middle camber (Mao et al., 2011); as a result, it is possible to precisely control this process through manipulating current generation. Separation of the cathode electrode from the reaction chamber will minimize the effects of generated OH^- on iron catalysts and PS consumption. The specific objectives of this study are to: (1) investigate the feasibility of electrochemical control of PS activation by applying different positive currents on the sacrificial iron anode; (2) examine the kinetics of Fe^{2+} release to the reaction chamber and the interactions among PS, Fe^{2+}, and current; (3) evaluate the importance of slow-controlled release of Fe^{2+} by comparing with one-time dosage; and (4) demonstrate the degradation of a representative azo dye (Acid Orange, AO7) by the controlled PS activation.

2. Materials and methods

2.1. EMR setup

The schematic of the EMR is shown in Fig. 1, consisting of three chambers separated by two pieces of cation exchange membrane (CEM; the specification is listed in Table S1) with the same surface area of 5.3 cm^2/each (Membrane International Inc., Ringwood, NJ, USA). Each chamber contained 100-mL solution: the iron solution in the anode chamber, 100 mg L^{-1} AO7 in the middle (reaction) chamber, and 0.5-M NaCl solution in the cathode chamber. The concentration of AO7 (100 mg L^{-1}) was selected based on the range of the AO7 concentrations in the precious studies which varied from 20 mg L^{-1} to 250 mg L^{-1} (Cai et al., 2014; Mu et al., 2009; Yang et al., 2011). The Fe^{2+} solution was created by electrolyzing an iron anode (5 cm length × 1.9 cm width × 0.2 cm thickness) for 12 h and the anolyte was reused after each batch of experiment. Our measurement showed that the concentration of Fe^{2+} in the reused anolyte remained relatively constant throughout the experiments. The initial pH of the anolyte and the catholyte was adjusted to 2.0–2.2 using 1-M hydrochloric acid (HCl) to prevent iron oxide formation on the surface of the iron electrode and improve the cathode efficiency. The AO7 solution was mixed by using a

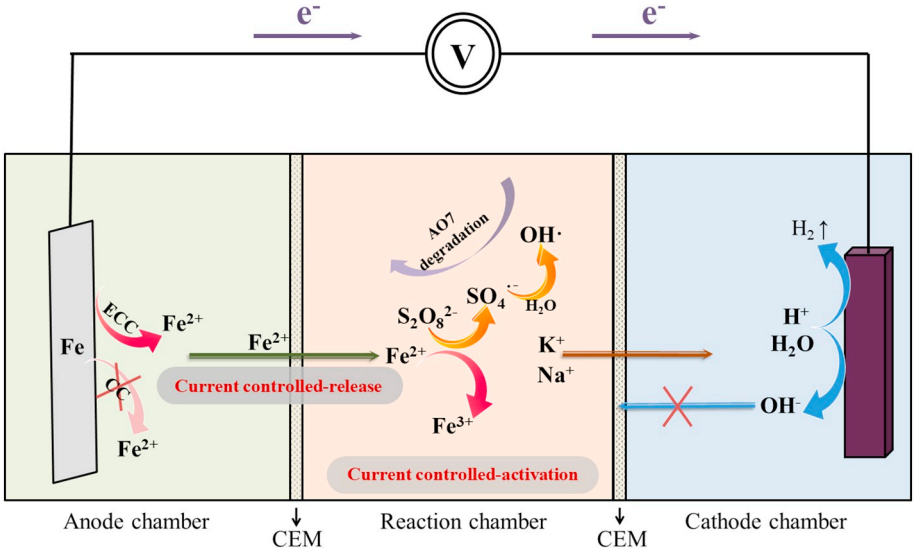

Fig. 1. Schematic of the electrochemical membrane reactor proposed in this study.

magnetic stir at 60 rpm. An external current was applied to the iron anode (positive pole) and a graphite cathode (4 cm length × 2.5 cm width × 1.3 cm thickness, negative pole) by using a power supply (HY3005F-3, Mastech Digital, Inc., Moon, PA, USA).

2.2. Experimental procedures

The experiments of the precise control of electrochemically activated persulfate (PCEAP) and Fe^{2+} release were conducted by applying positive and constant current of +10.0 mA, +20.0 mA, +30.0 mA, or +40.0 mA through the iron anode, with the initial addition of 3.0 g L^{-1} PS ($K_2S_2O_8$, 97%) in the reaction chamber, the pH of 3.0 and operation for 90 min.

To demonstrate the advantage of current-controlled slow release of Fe^{2+}, PS activation by one-time dosage was performed at the initial Fe^{2+} concentration of 100 mg L^{-1}, 200 mg L^{-1}, and 300 mg L^{-1} by adding $FeCl_2{\cdot}4H_2O$ (356 mg L^{-1}, 712 mg L^{-1}, and 1068 mg L^{-1}). The one-time dosage experiment was conducted in a 200-mL laboratory beaker containing 100-mL solution with a magnetic stir at 60 rpm, the same stirring speed as that in the EMR system. In this comparison test, the EMR system was operated at the current of +40.0 mA with pH of 3.0. Both one-time dosage and EMR experiments were conducted for 20 min.

For identification of (potentially) active radicals, we conducted quenching experiments by adding *tert*-butanol (TBA) or ethanol (EtOH) in the reaction chamber at scavenger concentrations of 111.0, 555.0 and 1110.0 mmol L^{-1}, which provided 10:1, 50:1 and 100:1 molar ratio of quencher to PS. The test conditions included 40.0 mA on the iron anode, 100 mg L^{-1} AO7, 3.0 g L^{-1} PS, initial pH of 3.0, and reaction for 90 min.

To examine the influence of PS addition, different initial concentrations of PS were added at 2.0 g L^{-1}, 2.5 g L^{-1}, 3.0 g L^{-1}, 3.5 g L^{-1} and 4.0 g L^{-1} (7.40 mmol L^{-1}, 9.25 mmol L^{-1}, 11.10 mmol L^{-1}, 12.95 mmol L^{-1} and 14.80 mmol L^{-1}). As a result, the dosage of PS was 26–52 times the molar ratio of AO7 (100 mg L^{-1}, that is 0.285 mmol L^{-1}). This ratio was lower than 50:1–200:1 reported in the previous literatures (Li et al., 2016; Lin et al., 2014; Shang et al., 2017b). The EMR system was run for 90 min for each batch experiment.

To investigate the effect of pH, NaOH (0.1 M) or HCl (0.1 M) was used to adjust initial middle chamber solution pH to 1.0, 3.0, 5.0, 7.0, 9.0 and 11.0, respectively. The solution in the middle chamber was adjusted to pH 3.0 for all the other tests. To study the effects of anions, Cl^- and SO_4^{2-} (the common electrolyte) were added at molar ratio of 10:1, 50:1 and 100:1 (NaCl to PS or Na_2SO_4 to PS).

Control experiments were performed without either PS addition or electrical current. All the experiments were conducted at room temperature and sampled periodically. All chemicals used in this study were purchased at an analytical grade from Fisher Chemical. All the data were obtained from triplicate experiments.

2.3. Analytical methods

The concentrations of PS and AO7 were analyzed by using a Thermo Scientific Genesys 20 spectrometer (Thermo Fisher Scientific, Inc., Rochester, NY, USA) at a wavelength of 352 nm and 484 nm, respectively, according to a previously described method (Liang et al., 2008; Wang et al., 2013). The concentrations of ferrous iron (Fe^{2+}) and total iron were determined by the 1,10-phenanthroline colorimetric method using a Hach DR/890 colorimeter (Hach Co., Loveland, USA) at the absorption of 510 nm. The concentrations of Na^+ and K^+ were quantified by using ion chromatography (Dionex LC20 ion chromatograph, Sunnyvale, CA, U.S.A.) equipped with an ED40 electrochemical detector. The solution pH was measured by a benchtop pH meter (Oakton Instruments, Vernon Hills, IL, USA). All the mathematical analyses were processed using the software Statistical Product and Service Solutions (SPSS). The relative contribution of $SO_4{\cdot}^-$ and ·OH to AO7 degradation was calculated according to the variation of rate constants (Ahmad et al., 2012; Liang et al., 2007; Yuan et al., 2014). The rate constant of AO7 degradation without a scavenging agent is denoted as k_0, the rate constant with addition of TBA scavenging ·OH only is denoted as k_{TBA}, and the rate constant with addition of EtOH scavenging both $SO_4{\cdot}^-$ and ·OH is denoted as k_{EtOH}. The contribution of ·OH is calculated as:

$$(k_0 - k_{TBA})/k_0 \times 100\% \quad (9)$$

$$(k_{TBA} - k_{EtOH})/k_0 \times 100\% \quad (10)$$

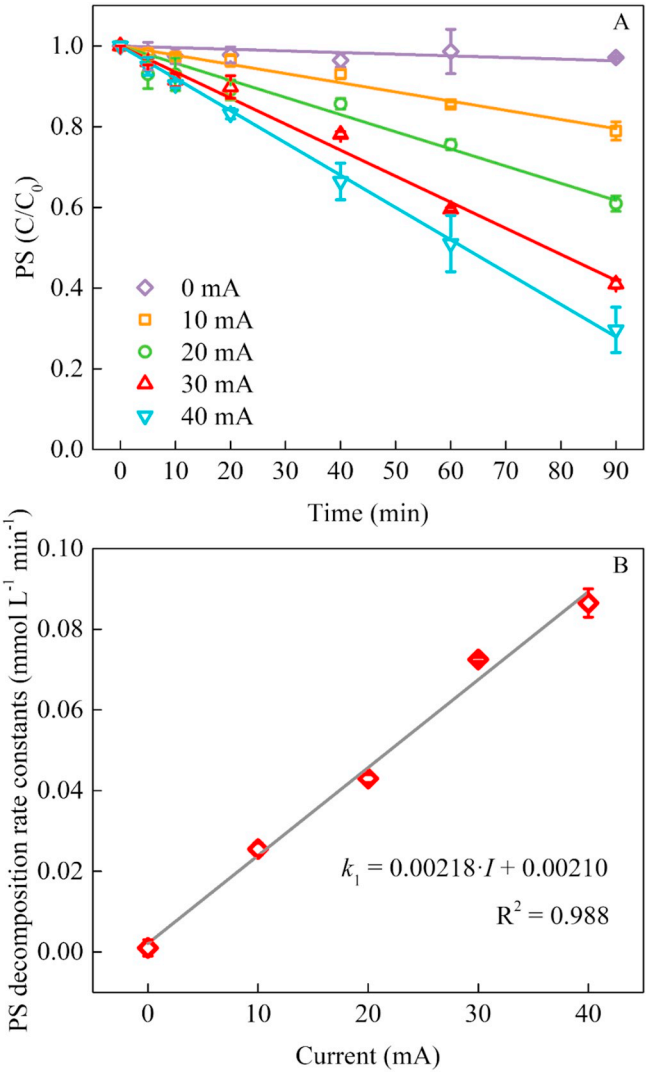

Fig. 2. Current stimulated persulfate decomposition with an iron electrode under different applied currents: (A) persulfate decomposition versus time; and (B) persulfate reaction rate constants versus current, the k_1 and I in the equation were the zero-order PS concentration decomposition rate constant (mmol L^{-1} min^{-1}) and the current (mA), respectively. Test conditions: 3.0 g L^{-1} PS, 100 mg L^{-1} AO7, and initial pH of 3.0.

3. Results and discussion

3.1. Current stimulated persulfate decomposition

PS activation is represented by its decomposition, which is in proportion to radical formation. In the EMR, the decomposition of PS increased as the applied current increased from 10.0 to 40.0 mA (Fig. 2A). The R^2 correlation coefficient was 0.970–0.999 for a linear relationship

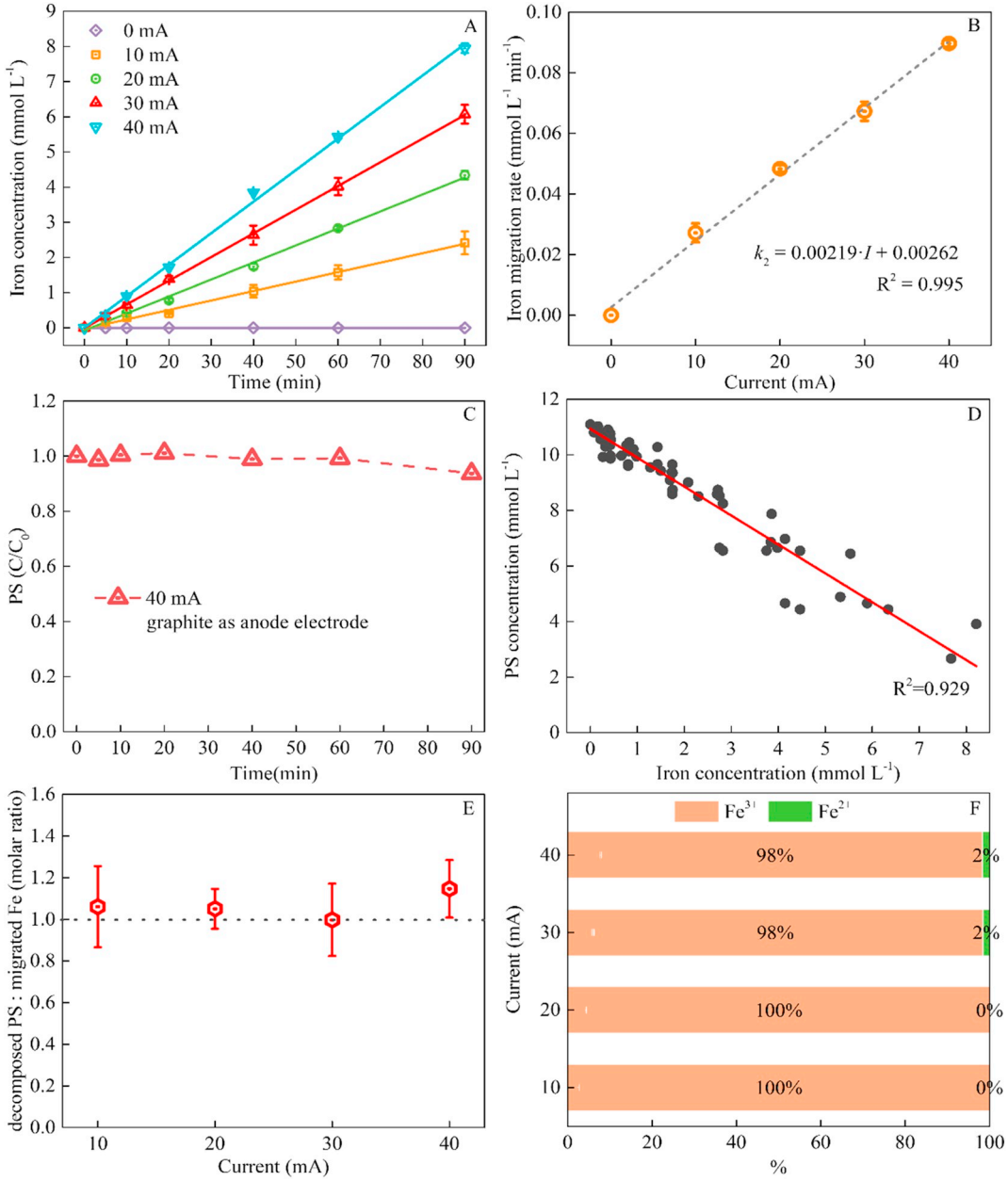

Fig. 3. Interactions between PS decomposition and iron migration: (A) the chemical kinetics of iron migration concentration; (B) iron migration rate as a function of current, the k_1 and I in the equation were the migration concentration rate (mmol L^{-1} min^{-1}) and the current (mA), respectively; (C) PS decomposition using graphite as anode electrode instead of iron electrode with current applied of 40.0 mA; (D) persulfate concentration as a function of iron migration concentration; (E) molar ratio of persulfate decomposition to iron migration in the middle chamber as a function of current density; and (F) distribution of Fe^{2+} and Fe^{3+} in the middle chamber at different current applied. Test conditions: 3.0 g L^{-1} PS, 100 mg L^{-1} AO7, and initial pH of 3.0.

of PS decomposition with time for all the applied currents (Table S2), suggesting that PS could be decomposed through a zero-order reaction. The equations of chemical kinetics of PS decomposition are shown in Box S1 and values of rate constants with respect to current are listed in Table S2. Unlike previous studies of membrane-less EAP systems in which uncontrollable PS decomposition occurred due to direct contact between zero-valent iron (iron electrode) and PS (Eq. (7)) (Matzek and Carter, 2017), PS was not activated in the absence of electrical current (0 mA) in the EMR. At the current of 10.0 mA, 20.0 mA, 30.0 mA and 40.0 mA, the PS decomposition percentage was 21.07 ± 2.27%, 39.07 ± 1.93%, 59.00 ± 1.01%, and 70.35 ± 5.61%, respectively (Fig. 2A). Fitting PS decomposition by zero-order kinetics results in decomposed concentration rate constants increasing from 0.026 ± 0.002 mmol L^{-1} min^{-1} at 10.0 mA to 0.043 ± 0.001 mmol L^{-1} min^{-1} at 20.0 mA, 0.073 ± 0.001 mmol L^{-1} min^{-1} at 30.0 mA, and then 0.087 ± 0.004 mmol L^{-1} min^{-1} at 40.0 mA. The current-dependent control of PS decomposition followed a linear correlation between PS decomposition rate constants and the applied currents (R^2 = 0.988), and the relationship equation is shown in the Fig. 2B. All those results suggested that the PS composition could be quantitatively controlled by applied current.

3.2. Current controlled Fe^{2+} release

Theoretically, PS decomposes by accepting electrons from electron donors such as a cathode electrode or Fe^{2+}, and the latter can be produced from a sacrificial anode electrode by ECC or CC in a conventional EAP process (Matzek and Carter, 2016). Herein, Fe^{2+} ions produced from ECC

of the anode iron electrode that acted as the only resource of electrons (Eq. (6)). A linear relationship was observed between migrated Fe^{2+} across CEM and reaction time at all the applied currents (Fig. 3A), with R^2 values > 0.997 (Table S3). The equations of iron migrated Fe^{2+} concentration are shown in Box S2. The rate of Fe^{2+} migration (Yang and Cho, 2004; Casademont et al., 2008) was 0.027 ± 0.003 mmol L^{-1} min^{-1}, 0.048 ± 0.001 mmol L^{-1} min^{-1}, 0.067 ± 0.003 mmol L^{-1} min^{-1}, and 0.090 ± 0.001 mmol L^{-1} min^{-1} at the current of 10.0 mA, 20.0 mA, 30.0 mA and 40.0 mA, respectively (Fig. 3B), following a linear relationship between Fe^{2+} migration rate and applied current (R^2 = 0.995). Therefore, the release rate of Fe^{2+}, i.e. acceleration or deceleration, and the Fe^{2+} concentration in the reaction chamber could also be controlled by applied current.

The current-driven Fe^{2+} migration from the anode chamber to the reaction chamber was the primary cause of PS decomposition, because PS could not be activated by current alone with a graphite anode electrode (Fig. 3C). The significant dependence of PS decomposition on current can be attributed to the current-dependent production of Fe^{2+}. In the middle (reaction) chamber, the average molar concentration of PS was in proportion to molar concentration of the migrated Fe^{2+} (R^2 = 0.929, Fig. 3D). The molar ratio of the decomposed PS to the migrated Fe^{2+} as a function of current was nearly 1:1 at all the applied currents (Fig. 3E). The waste of radicals consumed by excess Fe^{2+} (Eq. (5)) would result in a molar ratio of the decomposed PS to the migrated Fe^{2+} lower than one (Matzek and Carter, 2017). In addition, the distribution of iron in the reaction chamber showed that the iron species were mostly in the form of Fe^{3+} (Fig. 3F), indicating that almost all the migrated Fe^{2+} was effectively used to activate PS and transformed to Fe^{3+}. This suggests that PS activation has followed a relationship that one mole of Fe^{2+} activates one mole of PS with production of both one mole ferric iron (Fe^{3+}) and one mole active radical according to Eq. (4). Thus, it is reasonable to conclude that the proposed EMR system could maximize the utilization of both Fe^{2+} and PS.

3.3. Advantages of current-controlled slow release of Fe^{2+}

Current generation can realize slow release of Fe^{2+} ions to the reaction chamber, and the benefit of this slow release was evaluated by comparing the EMR to one-time dosage of Fe^{2+} at different concentrations for both PS decomposition and AO7 removal. Increasing the one-time dosage of Fe^{2+} from 100 to 200 mg L^{-1} improved AO7 removal, because a higher Fe^{2+} concentration could react with more PS and thus generate more radicals to degrade AO7. Further increasing the Fe^{2+} concentration to 300 mg L^{-1} did not achieve significant enhancement, compared to that of 200 mg L^{-1}, likely due to that the decomposable PS and AO7 degradation percentage approached the maximum with 200 mg L^{-1} (p > 0.05, one-tailed two-sample t-test with unequal variance at α = 0.05 for all the following statistical tests, the detail algorithm showed in Supplementary material). The EMR system achieved a migrated Fe^{2+} concentration of 100 mg L^{-1} at 20 min under 40.0 mA and with a rate of 0.090 ± 0.001 mmol L^{-1} min^{-1}. The EMR-based slow-release Fe^{2+} process achieved much higher AO7 removal percentage (95.7 ± 0.7%) and PS decomposition (1.86 ± 0.14 mmol L^{-1}) than the one-time dosage of 100 mg L^{-1} Fe^{2+} (69.2 ± 0.6% and 1.32 ± 0.12 mmol L^{-1}) (Fig. 4A). To reach a comparable AO7 removal percentage to that of the EMR-based slow-release process, the one-time dosage would need a much higher Fe^{2+} concentration (> 200 mg L^{-1}) to activate more PS, resulting in a higher PS concentration of 2.64 ± 0.52 mmol L^{-1} (Fig. 4A) required for radicals' generation. Consequently, degradation of one molar AO7 would consume 10.26 ± 1.98 mol of PS with the one-time dosage of 200 mg L^{-1} Fe^{2+}, much higher than 6.88 ± 0.51 mol of PS with the EMR-based slow-release of 100 mg L^{-1} Fe^{2+} (Fig. 4B). In addition, the one-time dosage activated 0.57 ± 0.01 mol – 0.74 ± 0.15 mol of PS per mole of Fe^{2+} (Fig. 4C); this ratio was lower than 1, indicating that 43% - 26% of the added

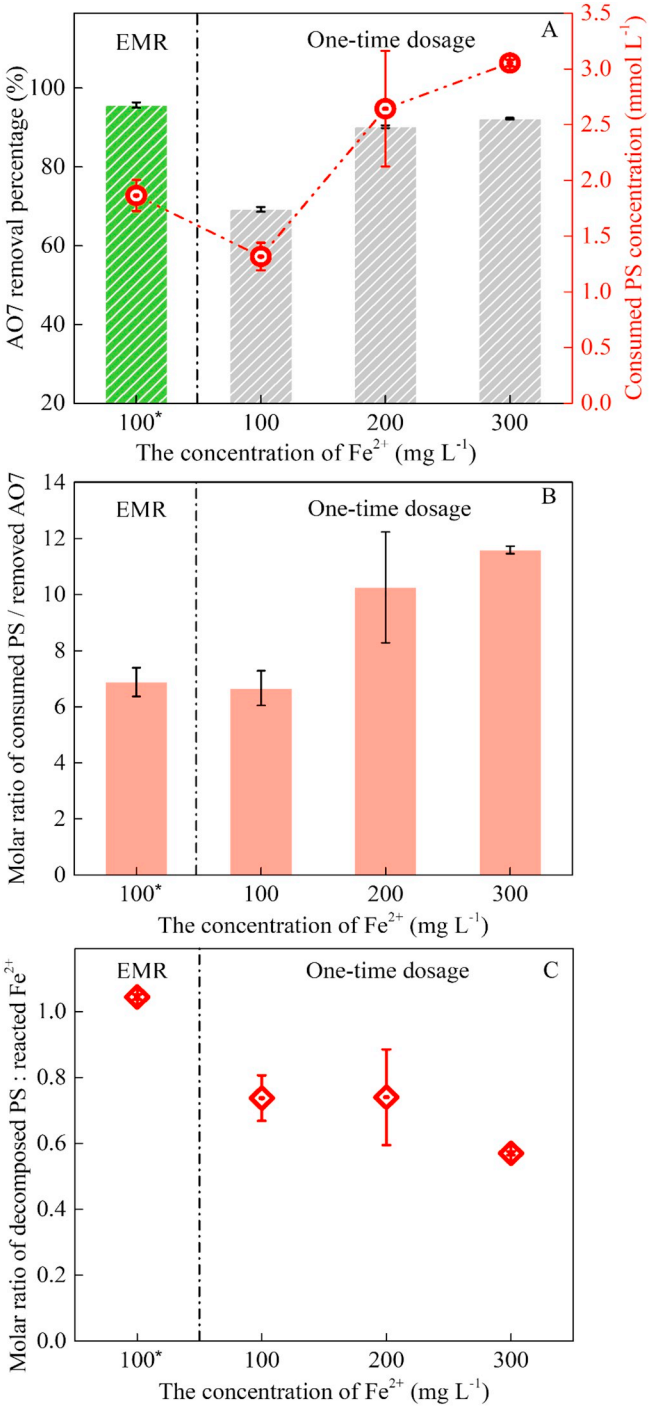

Fig. 4. Comparison between the EMR system and one-time dosage of Fe^{2+}: (A) AO7 removal percentage; (B) molar ratio of consumed PS to removed AO7; and (C) molar ratio of decomposed PS to reacted Fe^{2+}. Test conditions: 3.0 g L^{-1} PS, 100 mg L^{-1} AO7, initial pH of 3.0, and 40.0 mA. * means the concentration of migrated Fe^{2+} from the anode into the reaction chamber at 100 mg L^{-1}.

Fe^{2+} was wasted, likely by reacting with radicals as a scavenger (Eq. (5)) instead of activating PS as a catalyst. Therefore, the current controlled slow-release of Fe^{2+} in the EMR could minimize the waste of both reagents and generated radicals.

3.4. Identification of (potentially) active radicals

The high degradation percentage of AO7 in the EMR system may be ascribed to oxidation by active radicals (Y. Liu et al., 2018). It is

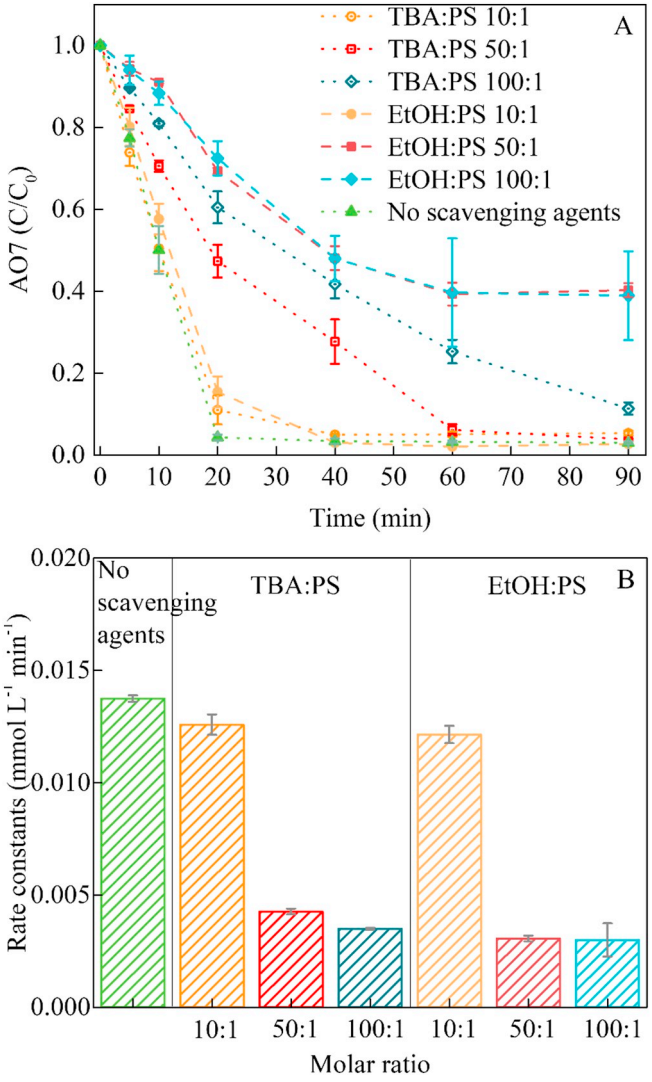

Fig. 5. Effects of radical scavenging agents on: (A) AO7 degradation; and (B) reaction rate constants at different molar ratio of TBA/EtOH and PS. Test conditions: 40.0 mA on the iron anode, 100 mg L^{-1} AO7, 3.0 g L^{-1} PS, and initial pH of 3.0.

generally recognized that $SO_4\cdot^-$ and ·OH are the responsible reactive intermediates produced from the process of PS activation by Fe^{2+}, and those radicals could play a key role in degradation of organic contaminants, as reported in numerous previous studies (Devi et al., 2016; Hung et al., 2016; Pan et al., 2018). To verify this, we conducted the quenching tests using EtOH and TBA to examine the roles of $SO_4^{\cdot-}$ and ·OH in AO7 removal (Anipsitakis and Dionysiou, 2004). The rate constant of ·OH formation from $SO_4\cdot^-$ in the presence of OH^- (5.5–7.5 × 10^7 mol^{-1} L s^{-1} (Hayon et al., 1972)) could be higher than the rate constant of EtOH with $SO_4\cdot^-$ (1.6 × 10^7 mol^{-1} L s^{-1} (Ye et al., 2018)). Thus, ·OH should be formed first and then quenched by EtOH. EtOH scavenges both ·OH and $SO_4\cdot^-$ with similar rate constants, while TBA is considered as the ·OH scavenger (Table S4) (Ghanbari and Moradi, 2017). The inhibition of AO7 degradation kinetics by using 10:1, 50:1 and 100:1 M ratio of TBA:PS was shown in Fig. 5A. The quenching effect of TBA was not strong at a relatively low ratio of 10:1, as demonstrated by the similar behavior of C/C_0 of AO7 to that without scavenger addition. Increasing the amount of TBA to 50:1 or 100:1 has clearly inhibited the AO7 removal, for example 52.7 ± 4.0% (50:1) or 39.5 ± 3.9% (100:1) at 20 min. To reach a high AO7 removal percentage, a longer reaction time of 60 min for 50:1 (93.8 ± 1.4%) or 90 min for 100:1 (88.6 ± 1.5%) would be needed (Fig. 5A). According to the pre-experiment, the rate constant of AO7 degradation with TBA:PS at 150:1 was similar to that at 100:1, indicating that the TBA:PS at the molar ratio of 100:1 was sufficient to scavenge ·OH. The rate constant of AO7 degradation without scavenging agents and with 100:1 of TBA:PS were 0.0138 ± 0.0001 mmol L^{-1} min^{-1} and 0.0035 ± 0.0001 mmol L^{-1} min^{-1}, respectively (Fig. 5B). The contribution of ·OH could be calculated by the inhibition of TBA because TBA preferentially quenching ·OH but not for $SO_4\cdot^-$. Thus, the relative contribution of ·OH was calculated to be 74.6%.

The addition of EtOH:PS at a low molar ratio of 10:1 had little effect on AO7 degradation, similar to that with TBA addition. The degradation percentage of AO7 decreased to 59.74 ± 1.71% and 61.10 ± 10.86%, respectively, when the addition of ethanol:PS increased to at 50:1 and 100:1 (Fig. 5A). The rate constants were 0.0031 ± 0.0001 mmol L^{-1} min^{-1} and 0.030 ± 0.0007 mmol L^{-1} min^{-1} with the addition of ethanol at 50:1 and 100:1, respectively (Fig. 5B), indicating that the EtOH was sufficient to scavenge ·OH and $SO_4\cdot^-$. The difference between the inhibition by the addition of TBA and EtOH can be attributed to different ability of quenchers to suppress ·OH and $SO_4\cdot^-$, which would reveal the contribution of $SO_4\cdot^-$. It was estimated that the relative contribution of $SO_4\cdot^-$ was only 3.6%, suggesting that ·OH which was produced from $SO_4\cdot^-$ (Eqs. (1) and (2)) during the activated persulfate oxidation might have played a much more significant role than $SO_4\cdot^-$ in the AO7 degradation. This phenomenon may be caused by the fast transformation from $SO_4\cdot^-$ to ·OH in both neutral and alkaline conditions (Eqs. (1) and (2)). The sum of contributions of ·OH and $SO_4\cdot^-$ was 78.2%, indicating the involvement of other degradation pathways, for example the radicals such as persulfate ($S_2O_8\cdot^-$), R· (organic), and ROO· (organo-peroxide) that could propagate from sulfate or hydroxyl radicals (Matzek et al., 2018).

3.5. Influence factors on AO7 degradation in the EMR

The EMR system was further evaluated for AO7 degradation affected by key operating factors including current, PS addition, pH, and anions. As expected, no obvious removal of AO7 was observed in the absence of current (Fig. S1). Current generation has stimulated the removal of AO7 and achieved the improved removal percentage from 27.3 ± 0.4% to 95.7 ± 0.7% (t = 20 min) when current increased from 10.0 to 40.0 mA (Fig. 6A). The removal rate became lower when a lower current was applied (Chen and Huang, 2015) resulting in longer reaction time needed to achieve similar removal percentage of AO7 (95.8 ± 0.8%, 95.2 ± 1.5% and 92.7 ± 0.2%) (Fig. 6A). The chemical kinetics of AO7 degradation followed the zero-order reaction under all the applied currents with R^2 > 0.981 (Table S5). The AO7 degradation rate constant was 0.031 ± 0.001 mmol L^{-1} min^{-1}, 0.071 ± 0.004 mmol L^{-1} min^{-1}, 0.120 ± 0.008 mmol L^{-1} min^{-1} and 0.137 ± 0.001 mmol L^{-1} min^{-1} at 10.0 mA, 20.0 mA, 30.0 mA and 40.0 mA, respectively (Fig. 6A inset). It was found that the AO7 degradation rate constants as a function of current also followed a zero-order mechanism with R^2 = 0.979, with the relationship equation shown in Box S4. Thus, the AO7 degradation can also be precisely manipulated by current generation in the EMR.

The effect of PS addition on AO7 degradation was not linear, with 3.0 g L^{-1} identified as a favorable concentration for AO7 degradation having a rate constant of 0.014 ± 0.0001 mmol L^{-1} min^{-1} (Fig. 6B, inset). At that concentration, the molar ratio of PS addition to AO7 degradation was 39:1, much lower than that of previous studies (varied from 100:1 up to 280:1) (Li et al., 2016; Lin et al., 2014; Shang et al., 2017a, 2017b; J. Wang et al., 2017; Yang et al., 2011), suggesting that PS reagent could be greatly reduced by using the EMR system. With the PS addition of 3.0 g L^{-1}, the molar ratio of the decomposed PS to the degraded AO7 was 6.83 ± 0.57:1, and the molar ratio of the decomposed PS to the migrated Fe was 1.17 ± 0.09:1 (Fig. S2A). A higher PS

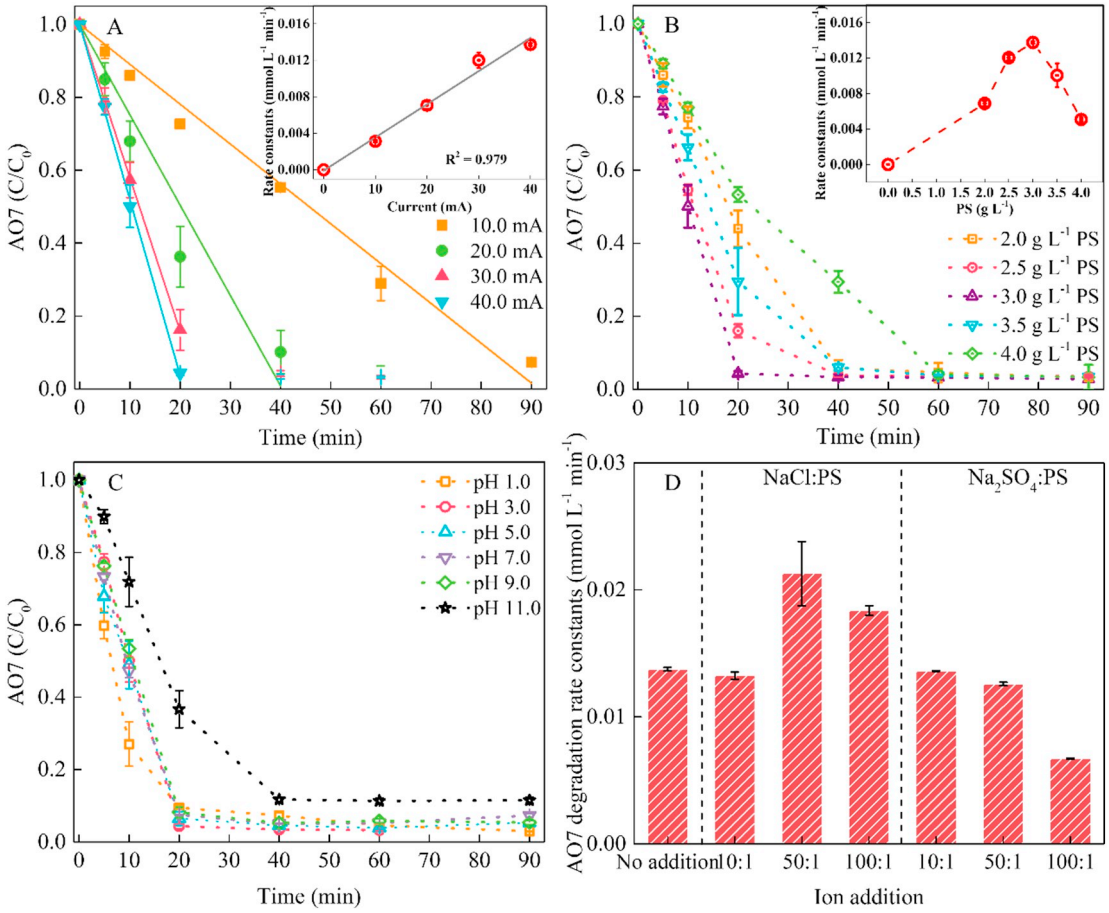

Fig. 6. Influence of (A) applied current; (B) PS dosage; (C) initial pH; and (D) background electrolyte (Cl^- or SO_4^{2-}) on degradation of AO7. Inse1ts show the correlation of AO7 degradation rate constants with either current or PS concentration.

dosage would consume more PS (Fig. S2B) and would generate more radicals. When PS dosage was higher than 3.0 g L^{-1}, a lower molar ratio of the decomposed PS to the migrated Fe^{2+} was obtained, indicating that more Fe^{2+} would be needed to active PS, thereby decreasing the PS activation rate and resulting in a lower AO7 degradation rate constant. In the previous studies of AO7 degradation by PS, the PS dosage was ranged from 100:1 to 280:1 (molar ratio of PS to AO7) (Lin et al., 2014; Shang et al., 2017a, 2017b; J. Wang et al., 2017). In the present EMR system, the PS dosage (11.10 mmol L^{-1}, or 3.0 g L^{-1}) was about 39 times that of AO7 (0.285 mmol L^{-1}); therefore, application of EMR could potentially save PS reagents compared to other PS-based treatment systems.

The solution pH decreased along with the reactions and the final pH was around 3.0 regardless of the initial pH variation between 3.0 and 11.0 (Fig. S3); this could be due to the formation of acid intermediates or consumption of hydroxyl during the reaction of ·OH derived from SO_4·$^-$ (Eqs. (1) and (2)) (Liang and Su, 2009). Because of the similar acidification within 10 min, the initial pH did not have obvious influence on AO7 degradation (Fig. 6C). This also indicated that radicals were formed from PS composition and could degrade AO7 at a wide range of initial pH values in the EMR system. However, the different pH led to the different concentrations of H^+ and OH^- and would impact the ·OH formation according to the Eqs. (1) and (2). It can be assumed that ·OH concentration may be dictated by the solution pH. The decomposition of PS was also determined at different pH, and the results showed that 11.66 ± 0.07%, 16.80 ± 1.26%, 11.87 ± 0.20%, 12.69 ± 0.34%, 10.97 ± 1.44% and 13.49 ± 0.25% PS was consumed to reach the similar removal percentage of AO7 at pH 1.0, 3.0, 5.0, 7.0, 9.0 and 11.0, respectively (Fig. S4).

Anions such as Cl^- and SO_4^{2-} are usually used as electrolyte components and may affect the AO7 degradation (Zhou et al., 2018). Fig. S5 showed that the effect of Cl^- addition on AO7 degradation was not obvious until a relatively high molar ratio NaCl:PS of 100:1. The slight increase in AO7 degradation rate constant (from 0.013 ± 0.0003 mmol L^{-1} min^{-1} to 0.021 ± 0.0025 mmol L^{-1} min^{-1} and 0.018 ± 0.0004 mmol L^{-1} min^{-1}, respectively, Fig. 6D) might be due to the reaction of Cl^- with SO_4·$^-$ ($k = 4.7 \times 10^8$ mol^{-1} L s^{-1}) (Qian et al., 2016) that yields reactive Cl· ($E^0 = 2.6$ V, Eq. (11)) (Zhu et al., 2018), and the generated Cl· reacts with Cl^- ($k = 8.5 \times 10^9$ mol^{-1} L s^{-1}) (Li et al., 2017) to produce oxidizing species of Cl_2·$^-$ (Eq. (12)), which can still degrade AO7. The Cl^- enhanced AO7 degradation percentage has also been reported in a previous study that the degradation rate constants increased from 0.0321 min^{-1} to 0.0328 min^{-1} with the addition of 1.85 mM Cl^- (J. Wang et al., 2017). The low addition of SO_4^{2-} (such as the molar ratio Na_2SO_4:PS of 10:1 and 50:1) had little effects on AO7 degradation, whereas the addition of 100:1 exhibited a negative effect with a decreased rate constant of 0.0067 ± 0.0001 mmol L^{-1} min^{-1} (Fig. 6D). The PS decomposition at the molar ratio Na_2SO_4:PS of 100:1 was 8.60 ± 0.36%, much lower than that without addition or with low addition ratio of 10:1 and 50:1 (16.80 ± 1.26%, 15.77 ± 1.57%, 14.71 ± 0.31%, respectively, $p < 0.05$) (Fig. S6). The less efficient activation of PS under a high SO_4^{2-} concentration should be attributed to the decrease of oxidative reduction potential of SO_4·$^-$/SO_4^{2-}, leading to the inhibition of AO7 removal (Zhou et al., 2016).

$$SO_4^{\bullet -} + Cl^- \rightarrow SO_4^{2-} + Cl^{\bullet} \quad (k = 4.7 \times 10^8\ mol^{-1}\ L\ s^{-1}) \tag{11}$$

$$Cl^{\bullet} + Cl^- \rightarrow Cl_2^{\bullet -} \quad (k = 8.5 \times 10^9\ mol^{-1}\ L\ s^{-1}) \tag{12}$$

The proposed EMR system could be a viable candidate for treating

various industrial wastewaters that contain recalcitrant contaminants. It was reported that the activated PS has been studied for treating groundwater, organic wastewater (such as benzotriazole, caffeine, phenols, BTEX, pharmaceutical, dyes, etc.), and specific wastewater including industrial discharge and landfill leachate (Matzek and Carter, 2016). Because of a generally small quantity of industrial wastewater (compared to that of municipal wastewater), the need for scaling up EMR system to a very large scale may be avoided and this could accelerate the application of the system. In addition, due to the recalcitrant nature of contaminants in some industrial wastewaters, the treatment may tolerate a relatively higher energy cost, which is a key factor of applying EMR system. Exploring the use of renewable energy such as solar energy could further reduce the operating expense of EMR system.

4. Conclusions

In this study, the precise control of persulfate activity was achieved by adjusting current applied to the iron electrode in an electrochemical membrane reactor. The following conclusions can be drawn based on the results:

- The current stimulated PS decomposition followed a zero-order reaction mechanism, and had a linear correlation with applied current. The presence of ion exchange membrane facilitated current-drive iron movement and avoided direct contact between the iron electrode and PS.
- Slow release of Fe^{2+} controlled by current in the EMR exhibited higher PS utilization efficiency and contamination degradation, compared to those with one-time dosage of Fe^{2+}.
- The Fe^{2+} induced PS activation could produce both $SO_4\cdot^-$ and ·OH radicals for degrading AO7. However, ·OH radicals might have played a more important role than $SO_4\cdot^-$ radicals.
- A linear relationship was observed between AO7 degradation rate constants and current. The PS concentration of $3.0\,g\,L^{-1}$ was optimal for AO7 degradation at the tested concentration. The initial solution pH had little influence on the degradation of AO7, whereas a high Cl^- addition could promote AO7 degradation and a high SO_4^{2-} addition had an inhibiting effect.

Declaration of Competing Interest

The authors declare that they have no known competing financial interests or personal relationships that could have appeared to influence the work reported in this paper.

Acknowledgements

This work was supported by a grant from Institute for Critical Technologies and Applied Science, Virginia Tech. Simiao Wu was financially supported by an award from China Scholarship Council (CSC).

Appendix A. Supplementary data

Supplementary materials include 4 boxes, 5 tables and 7 figures. Boxes showing the chemical kinetics of PS decomposition and iron migration; and equations of AO7 degradation rate constants as a function of current, and quenching by TBA and EtOH. Tables showing the rate constants of PS decomposition, Fe migration and AO7 degradation by current; and the quenching rate constants of TBA and EtOH. Figures showing AO7 degradation without current applied; PS decomposition under different PS addition, initial pH, and anions addition; pH variation under different initial pH; and anions effect on AO7 degradation. Supplementary data to this article can be found online at doi:https://doi.org/10.1016/j.envint.2019.105024.

References

Ahmad, M., Teel, A., S Furman, O., I Reed, J., J Watts, R., 2012. Oxidative and reductive pathways in iron-ethylenediaminetetraacetic acid–activated persulfate systems. J. Environ. Eng. 138, 411–418.
Al-Shamsi, M.A., Thomson, N.R., 2013. Treatment of organic compounds by activated persulfate using nanoscale zerovalent iron. Ind. Eng. Chem. Res. 52 (38), 13564–13571.
An, D., Westerhoff, P., Zheng, M., Wu, M., Yang, Y., Chiu, C.-A., 2015. UV-activated persulfate oxidation and regeneration of NOM-saturated granular activated carbon. Water Res. 73, 304–310.
Anipsitakis, G.P., Dionysiou, D.D., 2004. Radical generation by the interaction of transition metals with common oxidants. Environ. Sci. Technol. 38 (13), 3705–3712.
Cai, C., Wang, L., Gao, H., Hou, L., Zhang, H., 2014. Ultrasound enhanced heterogeneous activation of peroxydisulfate by bimetallic Fe-Co/GAC catalyst for the degradation of acid orange 7 in water. J. Environ. Sci. 26 (6), 1267–1273.
Cai, C., Zhang, Z., Zhang, H., 2016. Electro-assisted heterogeneous activation of persulfate by Fe/SBA-15 for the degradation of Orange II. J. Hazard. Mater. 313, 209–218.
Casademont, C., Farias, M., Pourcelly, G., Bazinet, L., 2008. Impact of electrodialytic parameters on cation migration kinetics and fouling nature of ion-exchange membranes during treatment of solutions with different magnesium/calcium ratios. J. Membr. Sci. 325, 570–579.
Chen, W.-S., Huang, C.-P., 2015. Mineralization of aniline in aqueous solution by electrochemical activation of persulfate. Chemosphere 125, 175–181.
Chen, Y.-d., Ho, S.-H., Wang, D., Wei, Z.-s., Chang, J.-S., Ren, N.-q., 2018. Lead removal by a magnetic biochar derived from persulfate-ZVI treated sludge together with one-pot pyrolysis. Bioresour. Technol. 247, 463–470.
Devi, P., Das, U., Dalai, A.K., 2016. In-situ chemical oxidation: principle and applications of peroxide and persulfate treatments in wastewater systems. Sci. Total Environ. 571, 643–657.
Ghanbari, F., Moradi, M., 2017. Application of peroxymonosulfate and its activation methods for degradation of environmental organic pollutants: review. Chem. Eng. J. 310, 41–62.
Han, D., Wan, J., Ma, Y., Wang, Y., Li, Y., Li, D., Guan, Z., 2015. New insights into the role of organic chelating agents in Fe(II) activated persulfate processes. Chem. Eng. J. 269, 425–433.
Hayon, E., Treinin, A., Wilf, J., 1972. Electronic spectra, photochemistry, and autoxidation mechanism of the sulfite-bisulfite-pyrosulfite systems. SO2-, SO3-, SO4-, and SO5- radicals. J. Am. Chem. Soc. 94 (1), 47–57.
Hung, C.-M., Chen, C.-W., Liu, Y.-Y., Dong, C.-D., 2016. Decolorization of methylene blue by persulfate activated with FeO magnetic particles. Water Environ. Res. 88 (8), 675–686.
Jawad, A., Lang, J., Liao, Z., Khan, A., Ifthikar, J., Lv, Z., Long, S., Chen, Z., Chen, Z., 2018. Activation of persulfate by CuOx@Co-LDH: a novel heterogeneous system for contaminant degradation with broad pH window and controlled leaching. Chem. Eng. J. 335, 548–559.
Jo, W.-K., Tayade, R.J., 2014. New generation energy-efficient light source for photocatalysis: LEDs for environmental applications. Ind. Eng. Chem. Res. 53 (6), 2073–2084.
Kamagate, M., Amin Assadi, A., Kone, T., Coulibaly, L., Hanna, K., 2018. Activation of persulfate by irradiated laterite for removal of fluoroquinolones in multi-component systems. J. Hazard. Mater. 346, 159–166.
Kim, C., Ahn, J.-Y., Kim, T.Y., Shin, W.S., Hwang, I., 2018. Activation of persulfate by nanosized zero-valent Iron (NZVI): mechanisms and transformation products of NZVI. Environ. Sci. Technol. 52 (6), 3625–3633.
Lee, Y.-C., Lo, S.-L., Chiueh, P.-T., Chang, D.-G., 2009. Efficient decomposition of perfluorocarboxylic acids in aqueous solution using microwave-induced persulfate. Water Res. 43 (11), 2811–2816.
Li, J., Ren, Y., Lai, L., Lai, B., 2018. Electrolysis assisted persulfate with annular iron sheet as anode for the enhanced degradation of 2, 4-dinitrophenol in aqueous solution. J. Hazard. Mater. 344, 778–787.
Li, J., Dou, X., Qin, H., Sun, Y., Yin, D., Guan, X., 2019. Characterization methods of zerovalent iron for water treatment and remediation. Water Res. 148, 70–85.
Li, W., Orozco, R., Camargos, N., Liu, H., 2017. Mechanisms on the impacts of alkalinity, pH, and chloride on persulfate-based groundwater remediation. Environ. Sci. Technol. 51 (7), 3948–3959.
Li, X., Guo, W., Liu, Z., Wang, R., Liu, H., 2016. Fe-based MOFs for efficient adsorption and degradation of acid orange 7 in aqueous solution via persulfate activation. Appl. Surf. Sci. 369, 130–136.
Liang, C., Su, H.-W., 2009. Identification of sulfate and hydroxyl radicals in thermally activated persulfate. Ind. Eng. Chem. Res. 48 (11), 5558–5562.
Liang, C., Bruell, C.J., Marley, M.C., Sperry, K.L., 2004. Persulfate oxidation for in situ remediation of TCE. II. Activated by chelated ferrous ion. Chemosphere 55 (9), 1225–1233.
Liang, C., Wang, Z.-S., Bruell, C.J., 2007. Influence of pH on persulfate oxidation of TCE at ambient temperatures. Chemosphere 66 (1), 106–113.
Liang, C., Huang, C.-F., Mohanty, N., Kurakalva, R.M., 2008. A rapid spectrophotometric determination of persulfate anion in ISCO. Chemosphere 73 (9), 1540–1543.
Lin, H., Zhang, H., Hou, L., 2014. Degradation of C. I. acid orange 7 in aqueous solution by a novel electro/Fe3O4/PDS process. J. Hazard. Mater. 276, 182–191.
Liu, B., Qu, F., Chen, W., Liang, H., Wang, T., Cheng, X., Yu, H., Li, G., Van der Bruggen, B., 2017. Microcystis aeruginosa-laden water treatment using enhanced coagulation by persulfate/Fe(II), ozone and permanganate: comparison of the simultaneous and successive oxidant dosing strategy. Water Res. 125, 72–80.
Liu, N., Ding, F., Weng, C.-H., Hwang, C.-C., Lin, Y.-T., 2018. Effective degradation of

primary color direct azo dyes using Fe0 aggregates-activated persulfate process. J. Environ. Manag. 206, 565–576.
Liu, Y., Zhou, A., Gan, Y., Li, X., 2018. Roles of hydroxyl and sulfate radicals in degradation of trichloroethene by persulfate activated with Fe2+ and zero-valent iron: insights from carbon isotope fractionation. J. Hazard. Mater. 344, 98–103.
Lu, J., Dong, W., Ji, Y., Kong, D., Huang, Q., 2016. Natural organic matter exposed to sulfate radicals increases its potential to form halogenated disinfection byproducts. Sci. Total Environ. 50 (10), 5060–5067.
Mao, X., Ciblak, A., Amiri, M., Alshawabkeh, A.N., 2011. Redox control for electrochemical dechlorination of trichloroethylene in bicarbonate aqueous media. Environ. Sci. Technol. 45 (15), 6517–6523.
Matzek, L.W., Carter, K.E., 2016. Activated persulfate for organic chemical degradation: a review. Chemosphere 151, 178–188.
Matzek, L.W., Carter, K.E., 2017. Sustained persulfate activation using solid iron: kinetics and application to ciprofloxacin degradation. Chem. Eng. J. 307, 650–660.
Matzek, L.W., Tipton, M.J., Farmer, A.T., Steen, A.D., Carter, K.E., 2018. Understanding electrochemically activated persulfate and its application to ciprofloxacin abatement. Environ. Sci. Technol. 52 (10), 5875–5883.
Mu, Y., Rabaey, K., Rozendal, R.A., Yuan, Z., Keller, J., 2009. Decolorization of azo dyes in bioelectrochemical systems. Environ. Sci. Technol. 43 (13), 5137–5143.
Oh, S.-Y., Kim, H.-W., Park, J.-M., Park, H.-S., Yoon, C., 2009. Oxidation of polyvinyl alcohol by persulfate activated with heat, Fe2+, and zero-valent iron. J. Hazard. Mater. 168 (1), 346–351.
Oh, W.-D., Dong, Z., Lim, T.-T., 2016. Generation of sulfate radical through heterogeneous catalysis for organic contaminants removal: current development, challenges and prospects. Appl. Catal. B Environ. 194, 169–201.
Pan, X., Yan, L., Qu, R., Wang, Z., 2018. Degradation of the UV-filter benzophenone-3 in aqueous solution using persulfate activated by heat, metal ions and light. Chemosphere 196, 95–104.
Pikaev, A.K., Zolotarevskii, V.I., 1967. Pulse radiolysis of aqueous solutions of sulfuric acid. Bull. Acad. Sci. USSR 16 (1), 181–182.
Pu, M., Guan, Z., Ma, Y., Wan, J., Wang, Y., Brusseau, M.L., Chi, H., 2018. Synthesis of iron-based metal-organic framework MIL-53 as an efficient catalyst to activate persulfate for the degradation of orange G in aqueous solution. Appl. Catal. A Gen. 549, 82–92.
Qian, Y., Guo, X., Zhang, Y., Peng, Y., Sun, P., Huang, C.-H., Niu, J., Zhou, X., Crittenden, J.C., 2016. Perfluorooctanoic acid degradation using UV–persulfate process: modeling of the degradation and chlorate formation. Environ. Sci. Technol. 50 (2), 772–781.
Rosenfeldt, E.J., Linden, K.G., Canonica, S., von Gunten, U., 2006. Comparison of the efficiency of OH radical formation during ozonation and the advanced oxidation processes O3/H2O2 and UV/H2O2. Water Res. 40 (20), 3695–3704.
Shang, K., Wang, X., Li, J., Wang, H., Jiang, N., Lu, N., Wu, Y., 2017a. Effect of persulfate on the degradation of acid orange 7 (AO7) by dielectric barrier discharge plasma. Top. Catal. 60 (12), 973–979.
Shang, K., Wang, X., Li, J., Wang, H., Lu, N., Jiang, N., Wu, Y., 2017b. Synergetic degradation of acid orange 7 (AO7) dye by DBD plasma and persulfate. Chem. Eng. J. 311, 378–384.
Silveira, J.E., Paz, W.S., Garcia-Muñoz, P., Zazo, J.A., Casas, J.A., 2017. UV-LED/ilmenite/persulfate for azo dye mineralization: the role of sulfate in the catalyst deactivation. Appl. Catal. B Environ. 219, 314–321.
Song, H., Yan, L., Jiang, J., Ma, J., Zhang, Z., Zhang, J., Liu, P., Yang, T., 2018. Electrochemical activation of persulfates at BDD anode: radical or nonradical oxidation? Water Res. 128, 393–401.
Tang, L., Liu, Y., Wang, J., Zeng, G., Deng, Y., Dong, H., Feng, H., Wang, J., Peng, B., 2018. Enhanced activation process of persulfate by mesoporous carbon for degradation of aqueous organic pollutants: electron transfer mechanism. Appl. Catal. B Environ. 231, 1–10.
Tian, J., Wu, C., Yu, H., Gao, S., Li, G., Cui, F., Qu, F., 2018. Applying ultraviolet/persulfate (UV/PS) pre-oxidation for controlling ultrafiltration membrane fouling by natural organic matter (NOM) in surface water. Water Res. 132, 190–199.
Vicente, F., Santos, A., Romero, A., Rodriguez, S., 2011. Kinetic study of diuron oxidation and mineralization by persulphate: effects of temperature, oxidant concentration and iron dosage method. Chem. Eng. J. 170 (1), 127–135.
Wang, J., Liao, Z., Ifthikar, J., Shi, L., Chen, Z., Chen, Z., 2017. One-step preparation and application of magnetic sludge-derived biochar on acid orange 7 removal via both adsorption and persulfate based oxidation. RSC Adv. 7 (30), 18696–18706.
Wang, L., Peng, L., Xie, L., Deng, P., Deng, D., 2017. Compatibility of surfactants and thermally activated persulfate for enhanced subsurface remediation. Environ. Sci. Technol. 51 (12), 7055–7064.
Wang, M., Liu, X., Pan, B., Zhang, S., 2013. Photodegradation of acid orange 7 in a UV/acetylacetone process. Chemosphere 93 (11), 2877–2882.
Wang, S., Wang, J., 2018. Trimethoprim degradation by fenton and Fe(II)-activated persulfate processes. Chemosphere 191, 97–105.
Wojnárovits, L., Takács, E., 2019. Rate constants of sulfate radical anion reactions with organic molecules: a review. Chemosphere 220, 1014–1032.
Wu, S., He, H., Li, X., Yang, C., Zeng, G., Wu, B., He, S., Lu, L., 2018. Insights into atrazine degradation by persulfate activation using composite of nanoscale zero-valent iron and graphene: performances and mechanisms. Chem. Eng. J. 341, 126–136.
Yang, C., Cho, S., 2004. The relationship between chloride migration rate for concrete and electrical current in steady state using the accelerated chloride migration test. Mater. Struct. 37, 456–463.
Yang, S., Yang, X., Shao, X., Niu, R., Wang, L., 2011. Activated carbon catalyzed persulfate oxidation of azo dye acid orange 7 at ambient temperature. J. Hazard. Mater. 186 (1), 659–666.
Ye, J., Zhou, P., Chen, Y., Ou, H., Liu, J., Li, C., Li, Q., 2018. Degradation of 1H-benzotriazole using ultraviolet activating persulfate: mechanisms, products and toxicological analysis. Chem. Eng. J. 334, 1493–1501.
Yin, R., Sun, J., Xiang, Y., Shang, C., 2018. Recycling and reuse of rusted iron particles containing core-shell Fe-FeOOH for ibuprofen removal: adsorption and persulfate-based advanced oxidation. J. Clean. Prod. 178, 441–448.
Yu, S., Gu, X., Lu, S., Xue, Y., Zhang, X., Xu, M., Qiu, Z., Sui, Q., 2018. Degradation of phenanthrene in aqueous solution by a persulfate/percarbonate system activated with CA chelated-Fe(II). Chem. Eng. J. 333, 122–131.
Yuan, S., Liao, P., Alshawabkeh, A.N., 2014. Electrolytic manipulation of persulfate reactivity by iron electrodes for trichloroethylene degradation in groundwater. Environ. Sci. Technol. 48 (1), 656–663.
Yun, E.-T., Yoo, H.-Y., Bae, H., Kim, H.-I., Lee, J., 2017. Exploring the role of persulfate in the activation process: radical precursor versus electron acceptor. Environ. Sci. Technol. 51 (17), 10090–10099.
Zhang, L., Ding, W., Qiu, J., Jin, H., Ma, H., Li, Z., Cang, D., 2018. Modeling and optimization study on sulfamethoxazole degradation by electrochemically activated persulfate process. J. Clean. Prod. 197, 297–305.
Zhang, Y., Zhang, Q., Dong, Z., Wu, l, Hong, J., 2018. Degradation of acetaminophen with ferrous/copperoxide activate persulfate: synergism of iron and copper. Water Res. 146, 232–243.
Zhen, G., Lu, X., Su, L., Kobayashi, T., Kumar, G., Zhou, T., Xu, K., Li, Y.-Y., Zhu, X., Zhao, Y., 2018. Unraveling the catalyzing behaviors of different iron species (Fe2+ vs. Fe0) in activating persulfate-based oxidation process with implications to waste activated sludge dewaterability. Water Res. 134, 101–114.
Zhou, T., Zou, X., Mao, J., Wu, X., 2016. Decomposition of sulfadiazine in a sonochemical Fe0-catalyzed persulfate system: parameters optimizing and interferences of wastewater matrix. Appl. Catal. B Environ. 185, 31–41.
Zhou, Y., Xiang, Y., He, Y., Yang, Y., Zhang, J., Luo, L., Peng, H., Dai, C., Zhu, F., Tang, L., 2018. Applications and factors influencing of the persulfate-based advanced oxidation processes for the remediation of groundwater and soil contaminated with organic compounds. J. Hazard. Mater. 359, 396–407.
Zhu, C., Zhu, F., Liu, C., Chen, N., Zhou, D., Fang, G., Gao, J., 2018. Reductive hexachloroethane degradation by $S_2O_8^{\bullet-}$ with thermal activation of persulfate under anaerobic conditions. Environ. Sci. Technol. 52 (15), 8548–8557.